ACS OMEGA

http://pubs.acs.org/journal/acsodf

Article

# MXene–Graphene Field-Effect Transistor Sensing of Influenza Virus and SARS-CoV-2

Yanxiao Li, Zhekun Peng, Natalie J. Holl, Md. Rifat Hassan, John M. Pappas, Congjie Wei, Omid Hoseini Izadi, Yang Wang, Xiangyang Dong, Cheng Wang, Yue-Wern Huang, DongHyun Kim,* and Chenglin Wu*

Cite This: *ACS Omega* 2021, 6, 6643–6653

Read Online

ACCESS | Metrics & More | Article Recommendations | Supporting Information

**ABSTRACT:** An MXene–graphene field-effect transistor (FET) sensor for both influenza virus and 2019-nCoV sensing was developed and characterized. The developed sensor combines the high chemical sensitivity of MXene and the continuity of large-area high-quality graphene to form an ultra-sensitive virus-sensing transduction material (VSTM). Through polymer linking, we are able to utilize antibody–antigen binding to achieve electrochemical signal transduction when viruses are deposited onto the VSTM surface. The MXene–graphene VSTM was integrated into a microfluidic channel that can directly receive viruses in solution. The developed sensor was tested with various concentrations of antigens from two viruses: inactivated influenza A (H1N1) HA virus ranging from 125 to 250,000 copies/mL and a recombinant 2019-nCoV spike protein ranging from 1 fg/mL to 10 pg/mL. The average response time was about ∼50 ms, which is significantly faster than the existing real-time reverse transcription-polymerase chain reaction method (>3 h). The low limit of detection (125 copies/mL for the influenza virus and 1 fg/mL for the recombinant 2019-nCoV spike protein) has demonstrated the sensitivity of the MXene–graphene VSTM on the FET platform to virus sensing. Especially, the high signal-to-viral load ratio (∼10% change in source-drain current and gate voltage) also demonstrates the ultra-sensitivity of the developed MXene–graphene FET sensor. In addition, the specificity of the sensor was also demonstrated by depositing the inactivated influenza A (H1N1) HA virus and the recombinant 2019-nCoV spike protein onto microfluidic channels with opposite antibodies, producing signal differences that are about 10 times lower. Thus, we have successfully fabricated a relatively low-cost, ultrasensitive, fast-responding, and specific inactivated influenza A (H1N1) and 2019-nCoV sensor with the MXene–graphene VSTM.

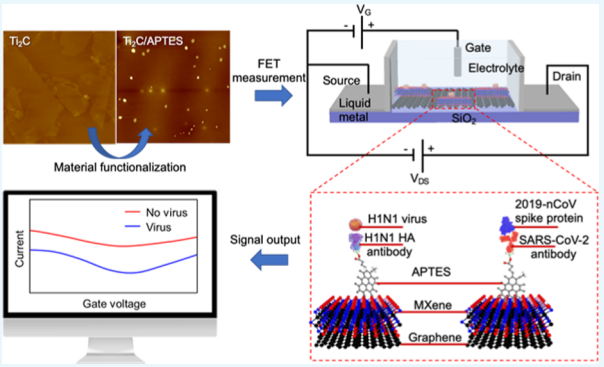




## 1. INTRODUCTION

The coronavirus disease recombinant 2019 (COVID-19) pandemic has encompassed more than 46.6M infected individuals and over 1.2M deaths worldwide. In October 2020, the total number of confirmed cases surpassed 9M in the United States alone and is still growing rapidly.[1] The U.S. economy contracted by almost a third (32.9%) during the second quarter of this year due to the pandemic, according to the U.S. Bureau of Economic Analysis.[2] Long-term side effects in internal organs, including the lungs and kidneys, are anticipated for recovered patients.[3−5] Point-of-care testing becomes critical in real-time detection and tracing of severe acute respiratory syndrome coronavirus 2 (SARS-CoV-2). However, the real-time detection and understandable data output desire a highly sensitive virus-sensing transduction material (VSTM) that can selectively sense the virus and transduce the sensing signal into electronic signals. Based on above reasons, two-dimensional (2D) materials including graphene are uniquely positioned as one of the best VSTMs for biosensing. Still, further improvement of the chemical reactivity of graphene-like VSTMs is needed to achieve higher selectivity and sensitivity for rapid and real-time biosensing.

Being one to a few atom-thin, 2D materials, including graphene, 2D transition-metal dichalcogenides (TMDs), and 2D transition-metal carbides (MXenes), have superior surface chemical sensitivity and lower sheet resistance than thin metal films.[6−10] This unique feature makes them ideal for electrochemical-based biosensors. Our recent work has shown that 2D material-based sensing devices can significantly enhance the detection limit of changes in chemical environments including corrosion and gas.[11]

Received: November 6, 2020
Accepted: January 22, 2021
Published: March 2, 2021

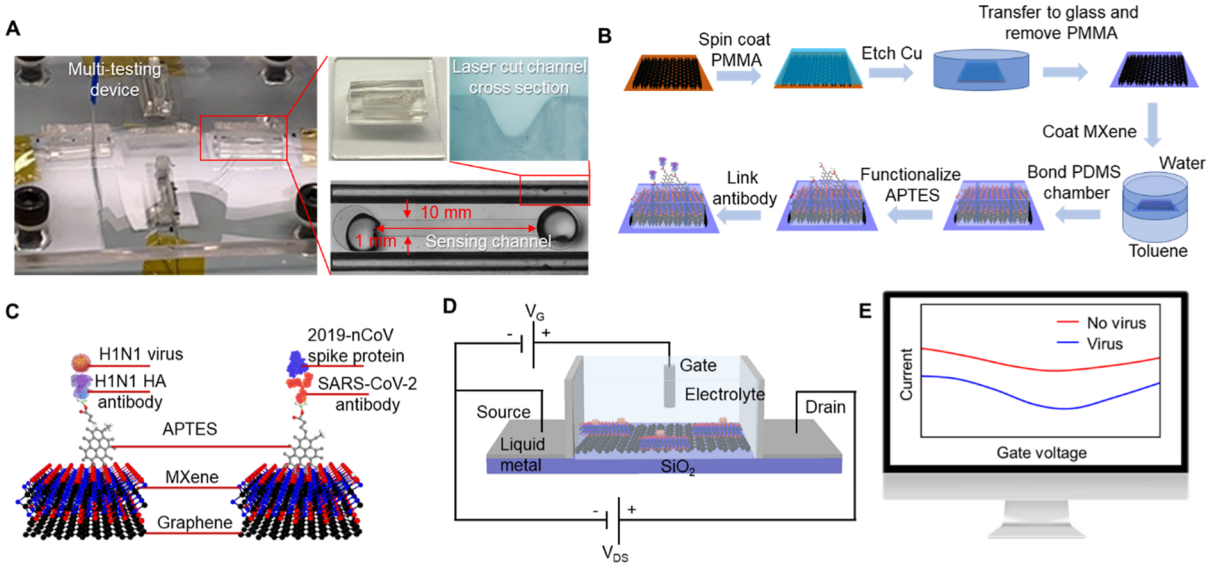


**Figure 1.** (A) Fabricated MXene–graphene FET sensor. (B) MXene–graphene VSTM deposition process, (C) illustration of antibody–antigen sensing mechanism, (D) FET circuit, and (E) change in drain-source current. Photograph: courtesy of "Yanxiao Li". Copyright 2020 and the image is of free domain.

Graphene is one of most investigated 2D materials for bio-sensing.[12−21] It can be functionalized with short polymer chains through non-covalent pi–pi interactions. Antibodies can then be attached to the polymer chains to immobilize targeted viral or bacterial antigens with high specificity for sensing. Naturally, the sensitivity of graphene-sensing materials heavily relies on van der Waals-type pi–pi interactions with the polymers. Being non-covalently bonded, this functionalization typically requires specific chemical groups in the polymer chains, which can cause low signal-to-noise ratios when the bonding is insufficient or weak.[22]

Recent progress has shown that MXenes can significantly improve the signal-to-noise ratios for electro-chemical sensing in comparison to graphene.[10] MXenes (typically in the form of $M_{n+1}X_n$) are a recently discovered family of 2D materials that consist of transition-metal elements ($M_{n+1}$) and carbon/nitrogen elements ($X_n$).[23,24] They are typically produced by chemical etching from their MAX phase precursors to remove the A element (typically either aluminum or silicon). As a result, MXenes typically have termination groups (oxygen, hydroxyl, fluorine, etc.) making them easier to be stably functionalized through covalent bonding.[25,26] In addition, their much higher conductivity in comparison with graphene gives them much higher signal-to-noise ratio in electro-chemical sensing.[27,28] In recent years, MXene has been actively investigated as a new electro-chemical sensing material for bio-sensing.[10] However, MXenes are typically in the form of overlapping flakes having a lateral size around 3 $\mu$m due to the chemical etching process.[29] This discontinuity may cause noisy signals in terms of sensing. In addition, a relatively thick film is normally formed to achieve sufficient overlapping for continuity, which greatly weakens its sensitivity. MXenes are highly conductive and have different functional groups (−H, −OH, −F) on the surface, which could form covalent bonding with polymers. However, with graphene, there are only pi–pi interactions. In addition, the small MXene flakes could be discontinuous and introduce a large initial resistance. The large-area continuous chemical vapor deposition (CVD)-grown graphene could solve these issues. In this work, we proposed utilizing an MXene on the graphene structure to combine the high chemical reactivity of MXene and the continuity of graphene to create an ultrasensitive VSTM. It should be noted that the average thickness of MXene on graphene has been kept below 10 nm to preserve its high chemical sensitivity.

Influenza viruses and coronaviruses are among the most common causes of infectious viral respiratory diseases. Real-time sensing of these viruses has attracted a significant amount of research interest, and various sensing mechanisms have been explored.[30−42] Among them, electro-chemical immunosensing has the fastest response time and the easiest signal transduction pathway for data interpretation. There are two critical processes for immunosensing platforms: the antibody–antigen binding and the chemical binding-induced electronic signals. For the antibody–antigen binding, antibodies specific to the virus alter the surface charge distribution of the VSTM after virus binding. The changed surface charge signal can then propagate to various electro-chemical signals. The electro-chemical signal transduction is commonly achieved using impedance and field-effect transistor (FET) approaches. The FET approach is ideally suited for virus sensing as it can easily accommodate the 2D VSTM film and produce an electronic output. Recent studies have also shown success using graphene FET sensing for influenza and SARS-CoV-2 virus.[43] However, due to the relatively low signal-to-noise ratio of the graphene-sensing material, the device lacks robustness and requires pre-processing of the virus sample. Therefore, a VSTM that has higher sensitivity and signal-to-noise ratio is needed to improve the robustness and allows minimum sample preparation, which will enable the automatic and real-time sensing of influenza and SARS-CoV-2 viruses. Here, we investigate a 2D MXene–graphene VSTM for FET immunosensing of influenza and SARS-CoV-2 viruses.

## 2. RESULTS AND DISCUSSION

**2.1. Sensor Fabrication.** The fabricated MXene–graphene FET sensor is shown in Figure 1A. The MXene–graphene sensing material was deposited onto a polydime-


https://dx.doi.org/10.1021/acsomega.0c05421
ACS Omega 2021, 6, 6643−6653

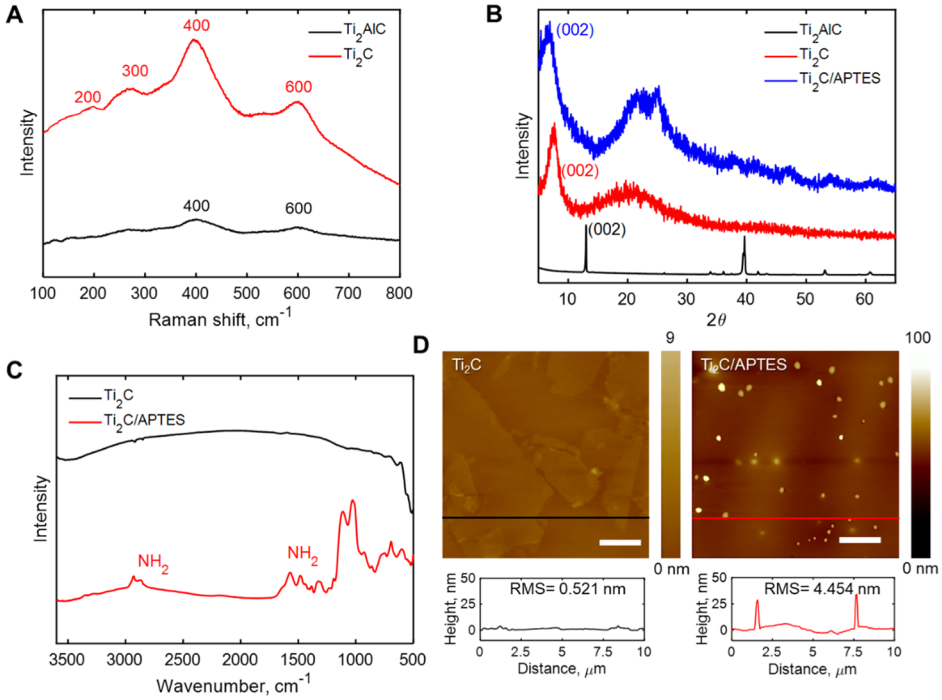


**Figure 2.** (A) Representative Raman spectra of the $Ti_2AlC$ MAX phase and $Ti_2C$ MXene. (B) XRD results for the $Ti_2AlC$ MAX phase, $Ti_2C$ MXene, and APTES-functionalized $Ti_2C$ MXene. (C) FTIR results for $Ti_2C$ MXene and APTES-functionalized $Ti_2C$ MXene. (D) AFM images of $Ti_2C$ MXene on graphene and APTES-functionalized $Ti_2C$ MXene on graphene. Scale bars in the image denote 2 $\mu$m.

thylsiloxane (PDMS) microfluidic channel with a length of 1 mm and a width of 10 mm (L × W). The source and drain electrodes were fabricated using a liquid metal (Galinstan) deposited onto laser-cut PDMS channels next to the main microfluidic channel. The main microfluidic channel was prepared using e-beam lithography and shadow-masked into the PDMS plate. A liquid gate was formed between the solution injected from the top opening of the microfluidic channel and the Ag/AgCl electrode. It should be noted that four sensors are integrated within one acrylic block for multi-virus sensing. The sensor fabrication details are explained in the Experimental Section.

The MXene–graphene VSTM was deposited in the following sequence. The CVD-grown, large-area, and monolayered graphene was first deposited onto the bottom surface of the microfluidic channel using the wet-transfer method.[44] MXene ($Ti_2C$) was subsequently deposited onto graphene using the interfacial deposition approach.[45] The MXene–graphene deposition process is illustrated in Figure 1B.

The antibody–antigen sensing mechanism is illustrated in Figure 1C. The surface of MXene–graphene VSTM was functionalized using (3-aminopropyl) triethoxysilane (APTES). The corresponding influenza A (H1N1) hemagglutinin (HA) polyclonal antibody and the SARS-CoV-2 spike antibody were then linked to APTES. When the inactivated influenza A (H1N1) virus and the recombinant 2019-nCoV spike protein bind with their corresponding antibodies, the associated change in surface charge was measured with the circuit shown in Figure 1D and reflected from the drain-source current–voltage response, as illustrated in Figure 1E.

**2.2. Characterization of MXene–Graphene.** The MXene–graphene VSTM was characterized using Raman spectrometry, Fourier-transform infrared (FTIR) spectroscopy, X-ray diffraction (XRD), and atomic force microscopy (AFM) after each step in the synthesis process. A comparison of characteristic Raman peaks of MXene ($Ti_2C$) at 200, 300, 400, and 600 $cm^{-1}$ with those of the MAX precursor ($Ti_2AlC$) at 400 and 600 $cm^{-1}$, as shown in Figure 2A indicates the successful removal of Al from $Ti_2AlC$. In addition, the d-spacing change from 0.68 to 1.15 nm, according to the XRD results of $Ti_2C$ and $Ti_2AlC$ (Figure 2B), also signifies the successful synthesis of $Ti_2C$ MXene. To confirm that the $Ti_2C$ surface was chemically functionalized with APTES, we conducted scans using FTIR spectroscopy, XRD, and AFM. The FTIR spectrum of APTES–MXene (Figure 2C) showed several new vibration peaks in comparison with those of MXene. For instance, new peaks at 1500 and 3350 $cm^{-1}$ (the stretching vibration mode of the free amine from APTES)[46] appeared in the FTIR spectrum of $Ti_2C$/APTES. This indicates the successful covalent coupling of APTES to $Ti_2C$ MXene. Since MXene has a 2D structure, the change in the interlayer distance after modification of silanes was also examined. The shift of the 002 peak of $Ti_2C$/APTES in the XRD pattern toward a smaller angle compared with that of $Ti_2C$ MXene (from 7.70 to 6.56°, Figure 2B) resulted in an increase of *d*-spacing to 1.35 nm. This could be attributed to the intercalation effect of APTES.[47] APTES could also be observed from AFM images (bright spots in Figure 2D). After APTES modification, the surface roughness (RMS) of MXene increased from 0.521 to 4.454 nm. In these contexts, APTES was successfully functionalized on the surface of MXene, which acted as a protein linker to immobilize antibodies onto the MXene surface. The grafting density of APTES on MXene is ~5% surface area ratio. The value is obtained by processing AFM images of APTES on MXene. At first, the AFM images were transferred to gray images and the gray values of different pixels were read out, then the amount of pixels at 255 gray value was calculated and divided using the total amount of pixels.


https://dx.doi.org/10.1021/acsomega.0c05421
ACS Omega 2021, 6, 6643–6653

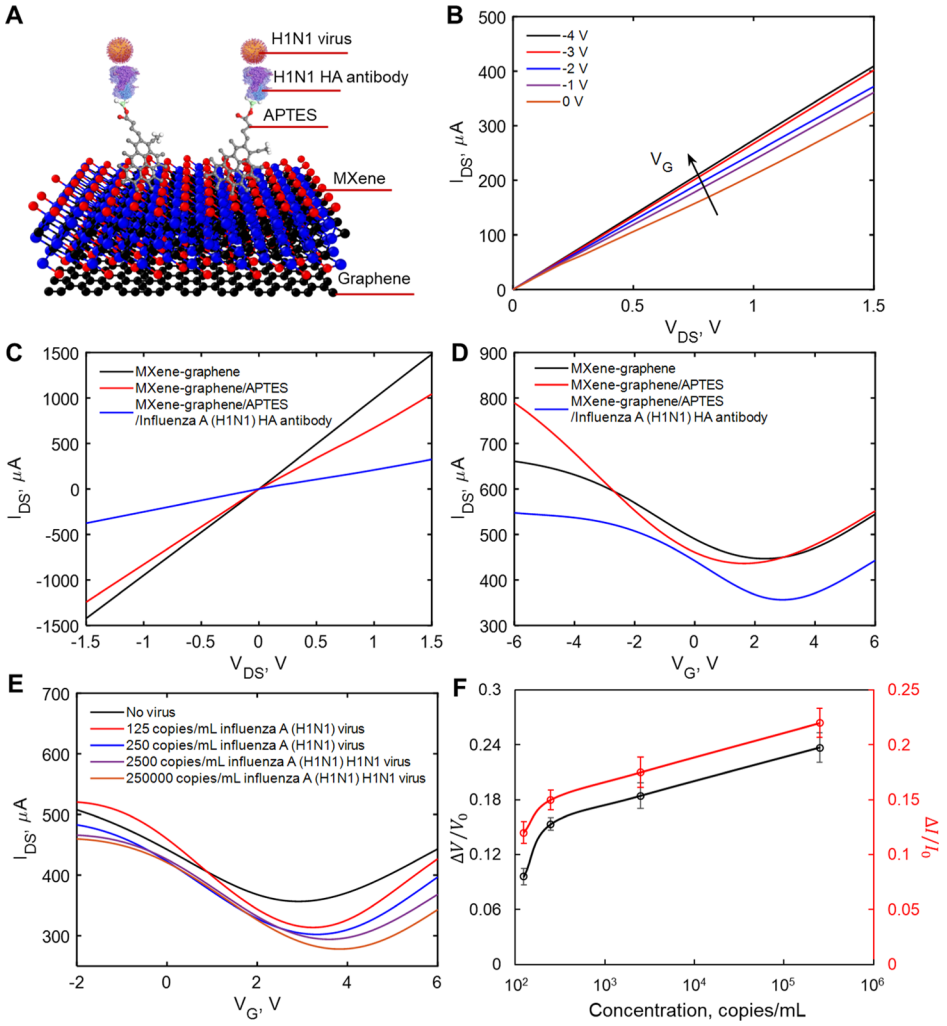


**Figure 3.** Electrical characterization of pristine, APTES-functionalized, and influenza A (H1N1) HA polyclonal antibody-immobilized MXene. (A) Diagram of the VSTM. (B) $I_{DS}$−$V_{DS}$ output curves of the antibody-conjugated FET with various gating voltages. (C) $I_{DS}$−$V_{DS}$ characteristics of the FET device of each modification process. (D) Measurement of transfer curves of the FET sensor in steps of antibody conjugation ($V_{DS}$ = 2 V). (E) $I_{DS}$−$V_G$ curves for different concentrations of inactivated influenza A (H1N1) virus. (F) Normalized gate-voltage shift and drain-source current change *vs* concentration of inactivated influenza A (H1N1) virus. The unit for voltage change is *V* and the unit for current change is μA. Errors bars for the eight tested sensors are given in terms of STDs ranging from ±0.007 to ±0.016 for the normalized neutral gate-voltage shift and from ±0.009 to ±0.014 for the normalized drain-source current change.

**2.3. Verification of FET and Virus Sensing.** To investigate the possibility of transducing an electrical signal with the FET sensor, we prepared a liquid-gated FET. The FET sensor was designed using a MXene−graphene surface conjugated to the influenza A (H1N1) HA polyclonal antibody or SARS-CoV-2 spike antibody inside the microfluidic channel and then covered with the phosphate-buffered saline (PBS; pH 7.4) that acted as the electrolyte to maintain an efficient gating effect. As illustrated in Figures 3A and 4A, the aqueous solution-gated FET system could detect the inactivated influenza A (H1N1) virus or recombinant 2019-nCoV spike protein based on changes in the channel surface potential and the corresponding effects on the electrical response.

We measured the transfer curves of the FET after each modification process (APTES functionalization and antibody immobilization), as shown in Figure 1B. Figures 3B and 4B show the drain-source current−voltage ($I_{DS}$−$V_{DS}$) output curves of the FET sensor as a function of gate voltage ($V_G$) over the range 0 to −4 V in steps of −1 V. $I_{DS}$ positively increased as $V_G$ negatively increased, corresponding to the predicted behavior of a p-type semiconductor.[43] Moreover, the linear $I_{DS}$−$V_{DS}$ curves exhibited highly stable Ohmic contact, indicating that the FET sensor provided a reliable electrical signal. For FET verification, we have tested two batches of sensors. For every batch of sensors, we tested four sensors for every pair of virus and antibody. All sensors showed consistent results.

To evaluate the presence of influenza A (H1N1) HA polyclonal antibody or SARS-CoV-2 spike antibody on the MXene surface, we carried out electrical measurements. Figures 3C and 4C show $I_{DS}$−$V_{DS}$ curves of the FET device after APTES functionalization and immobilization of the antibody onto the MXene channel. Over the range of −1.5 to +1.5 V of $V_{DS}$ before and after attachment of APTES and the antibody, the slopes ($dI_{DS}/dV_{DS}$) decreased. These differences in slopes indicate the successful introduction of APTES, influenza A (H1N1) HA polyclonal antibody, or SARS-CoV-2 spike antibody. In addition, as shown in Figures 3D and 4D, after APTES functionalization, an obvious negative shift was observed in $I_{DS}$−$V_G$ curves due to the n-doping effect of the


https://dx.doi.org/10.1021/acsomega.0c05421
ACS Omega 2021, 6, 6643−6653

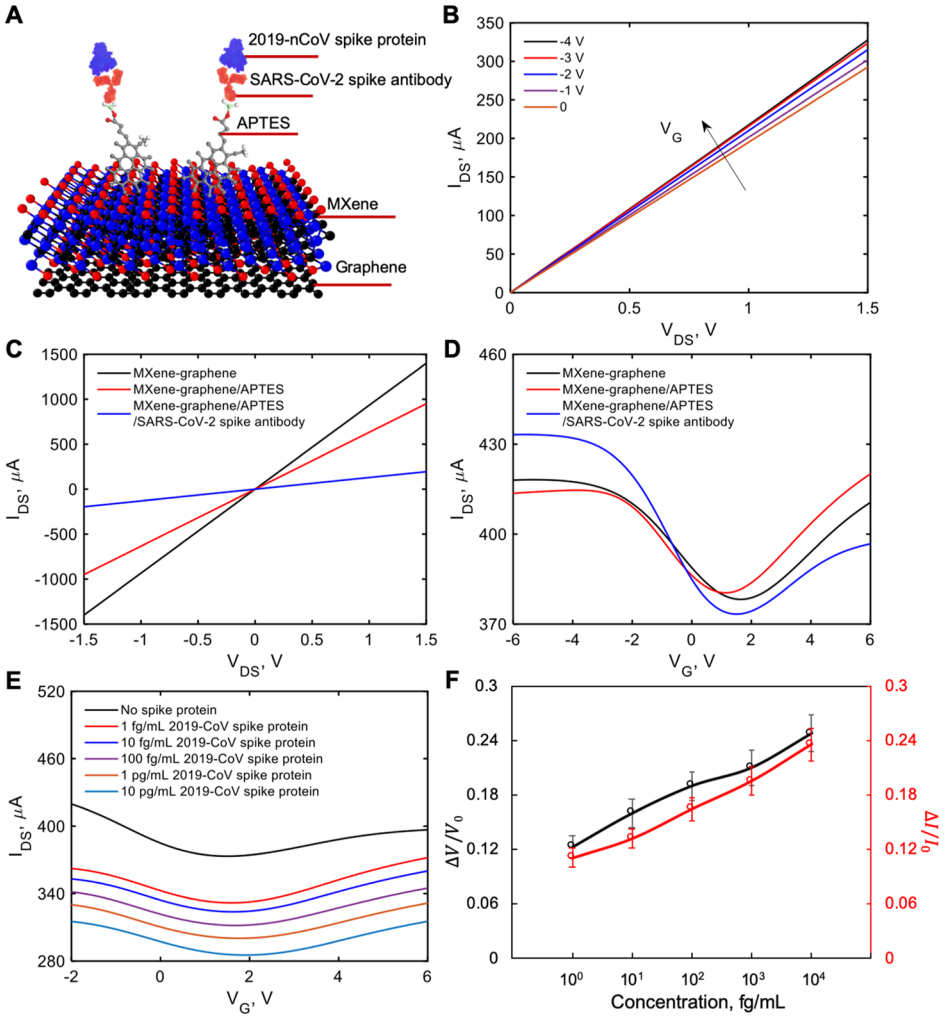


**Figure 4.** Electrical characterization of pristine, APTES-functionalized, and SARS-CoV-2 spike antibody-immobilized MXene. (A) Diagram of the VSTM. (B) $I_{DS}$−$V_{DS}$ output curves of the antibody-conjugated FET with various gating voltages. (C) $I_{DS}$−$V_{DS}$ characteristics of the FET device of each modification process. (D) Measurement of transfer curves of the FET sensor in steps of antibody conjugation ($V_{DS}$ = 2 V). (E) $I_{DS}$−$V_G$ curves for different concentrations of recombinant 2019-nCoV spike protein. (F) Normalized gate-voltage shift and drain-source current change *vs* concentration of recombinant 2019-nCoV spike protein. The unit for voltage change is *V* and the unit for current change is μA. Errors bars for the eight tested sensors are given in terms of standard deviation (STD) ranging from ±0.012 to ±0.02 for the normalized neutral gate-voltage shift and from ±0.01 to ±0.018 for the normalized drain-source current change.

amine group.[48] However, we noticed that the transfer curve shifted positively after immobilization of the antibody. We suspected that this was due to the negative charge of the antibody, which exerted a p-doping effect on MXene.

To investigate the performance of the MXene−graphene FET sensor, we evaluated the response of the sensor to different concentrations of inactivated influenza A (H1N1) virus or recombinant 2019-nCoV spike protein. First, we measured the sensor's limit of detection (LOD) for each antigen. The lowest concentrations the sensor responded to were 125 copies/mL inactivated influenza A (H1N1) virus or 1 fg/mL recombinant 2019-nCoV spike protein in PBS. Figures 3E and 4E show decreased $I_{DS}$ and a right shift of the lowest point in $I_{DS}$−$V_G$ curves ($V_{DS}$ = 2 V) with increased concentration of inactivated influenza A (H1N1) virus (from 125 to 250,000 copies/mL) or recombinant 2019-nCoV spike protein (from 1 fg/mL to 10 pg/mL). To investigate the sensitivity of the FET sensor, the detected electrical response signals were normalized as $\frac{\Delta V}{V_0} = \frac{V - V_0}{V_0}$ and $\frac{\Delta I}{I_0} = \frac{I_0 - I}{I_0}$, where *V* and *I* are the detected real-time gate voltage and drain-source current at the lowest point of $I_{DS}$−$V_G$ curves (i.e., neutral point); $V_0$ and $I_0$ are the gate voltage and drain-source current at the lowest point of $I_{DS}$−$V_G$ curves without inactivated influenza A (H1N1) virus or recombinant 2019-nCoV spike protein. The normalized neutral gate-voltage shift and drain-source current change *versus* concentration curves for the inactivated influenza A (H1N1) virus and the recombinant 2019-nCoV spike protein FET sensing process are shown in Figures 3F and 4F, respectively. The normalized neutral gate-voltage shift and the drain-source current change increased with the increase of inactivated influenza A (H1N1) virus or recombinant 2019-nCoV spike protein concentration. For voltage shift, the signal changes were 0.1 and 0.12 for the inactivated influenza A (H1N1) virus with a concentration of 125 copies/mL and the recombinant 2019-nCoV spike protein with a concentration of 1 fg/mL, respectively. The maximum concentrations tested for H1N1 and recombinant 2019-nCoV are 250,000 copies/mL and 10 pg/mL, with the corresponding shifts in the voltage of 0.24 and 0.25, respectively. For current


https://dx.doi.org/10.1021/acsomega.0c05421
ACS Omega 2021, 6, 6643−6653

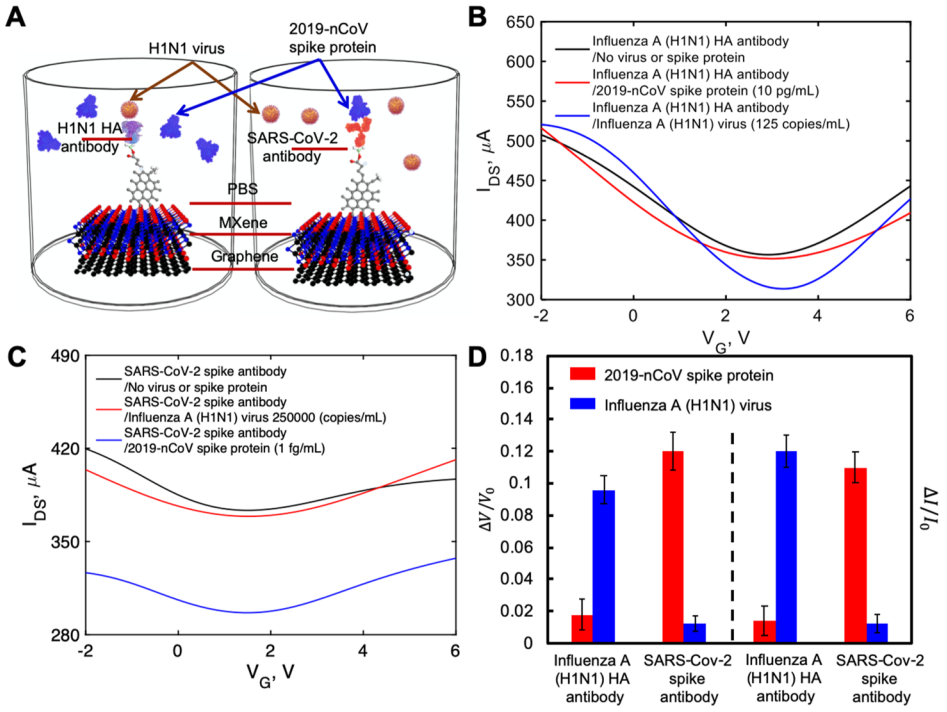


**Figure 5.** (A) Depiction of specific binding study inside PBS sample. $I_{DS}-V_G$ curves for (B) influenza A (H1N1) HA polyclonal antibody-immobilized FET sensor and (C) SARS-CoV-2 spike antibody-immobilized FET sensor. (D) Normalized gate-voltage shift and drain-source current changes with STDs in the specific binding study. The unit for voltage change is $V$ and the unit for current change is $\mu$A.

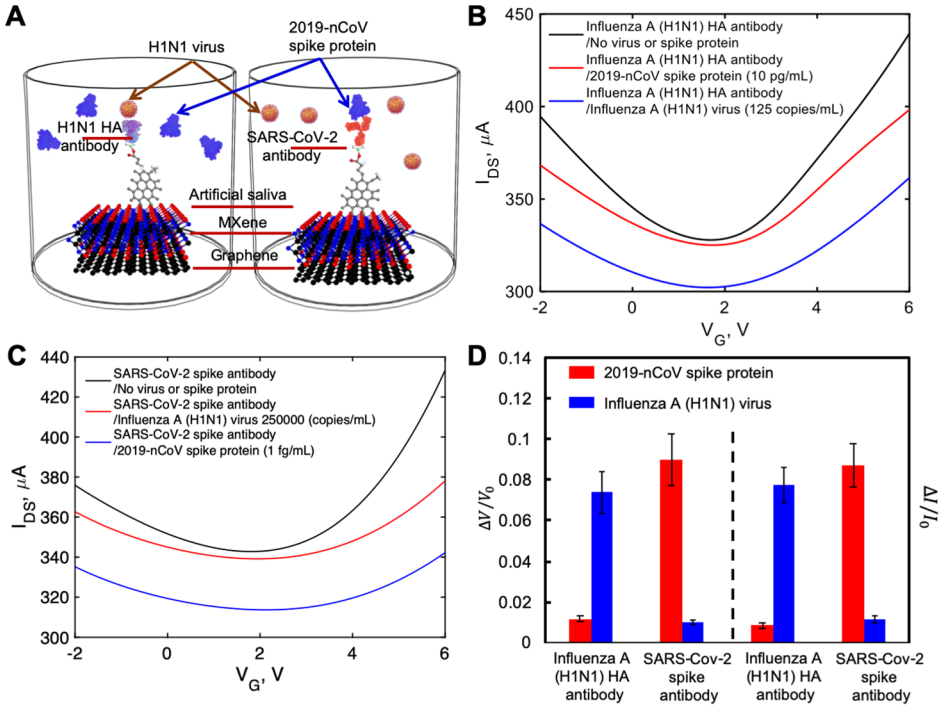


**Figure 6.** (A) Depiction of specific binding study inside artificial saliva sample. $I_{DS}-V_G$ curves for (B) influenza A (H1N1) HA polyclonal antibody-immobilized FET sensor and (C) SARS-CoV-2 spike antibody-immobilized FET sensor. (D) Normalized gate-voltage shift and drain-source current changes with STDs in specific binding study. The unit for voltage change is $V$ and the unit for current change is $\mu$A.

change, the signal changes were 0.12 and 0.11 for the inactivated influenza A (H1N1) virus with a concentration of 125 copies/mL and the recombinant 2019-nCoV spike protein with a concentration of 1 fg/mL, respectively. The maximum concentrations tested for H1N1 and recombinant 2019-nCoV are 250,000 copies/mL and 10 pg/mL, with the corresponding changes in current of 0.22 and 0.24, respectively. It should be noted that the normalized neutral gate-voltage shift and current change *versus* concentration plots shown in Figures 3f and 4f showed nonlinear proportional relationships, indicating a sound detection range of the developed sensor. The sensing response was determined by observing the time it took for the


https://dx.doi.org/10.1021/acsomega.0c05421
ACS Omega 2021, 6, 6643−6653

signal change, which was recorded from the sweeping data scanning at a rate of 1 $ns^{-1}$. The average response time for both viruses was about ∼50 ms.

**2.4. Specificity of Virus Sensing.** We investigated the specific binding of inactivated influenza A (H1N1) virus to the influenza A (H1N1) HA polyclonal antibody and the recombinant 2019-nCoV spike protein to the SARS-CoV-2 spike antibody, and thus, the specificity of our sensor, as shown in Figures 5A (inside PBS buffer) and 6A (inside artificial saliva). The FET sensor was functionalized with influenza A (H1N1) HA polyclonal antibody, and a recombinant 2019-nCoV spike protein sample was applied. As shown in Figure 5B, when using PBS buffer as the electrolyte, the FET sensor immobilized with influenza A (H1N1) HA polyclonal antibody showed very small response (0.018 ± 0.01 and 0.014 ± 0.009 for the neutral gate-voltage shift and drain-source current change, respectively, Figure 5D) to the recombinant 2019-nCoV spike protein, even with the largest concentration tested in our previous experiments (10 pg/mL). Likewise, as shown in Figure 5C the FET sensor functionalized with SARS-CoV-2 spike antibody showed very small response (0.013 ± 0.005 and 0.012 ± 0.001 for the gate-voltage shift and current change, respectively, Figure 5D) to inactivated influenza A (H1N1) virus (250,000 copies/mL), as shown in Figure 5C. The results obtained using artificial saliva as the electrolyte are also similar, as shown in Figure 5B,C,D. Small responses were observed when using unpaired antibody and virus.

However, there were significant signal changes when using antigens paired with sensors functionalized with the correct antibody. Using the lowest concentrations of antigens (125 copies/mL and 1 fg/mL for inactivated influenza A (H1N1) virus and recombinant 2019-nCoV spike protein, respectively) inside PBS buffer, the inactivated influenza A (H1N1) virus on the influenza A (H1N1) HA polyclonal antibody-immobilized FET sensor showed a 10-fold higher response (0.096 ± 0.009 and 0.12 ± 0.01 for the gate-voltage shift and drain-source current change, respectively, Figure 5D) than the highest concentration of recombinant 2019-nCoV spike protein with the same antibody. Similarly, using the recombinant 2019-nCoV spike protein on the SARS-CoV-2 spike antibody-immobilized FET sensor also produced an approximate 10-fold increase (0.122 ± 0.012 and 0.111 ± 0.01 for the gate-voltage shift and drain-source current change, respectively, Figure 5D) compared to that using the highest concentration of inactivated influenza A (H1N1) virus. The responses are a little smaller (0.074 ± 0.010 and 0.077 ± 0.009 for the gate-voltage shift and drain-source current change, respectively, Figure 6D) when using the lowest concentrations of inactivated influenza A (H1N1) virus inside artificial saliva. Smaller responses (0.09 ± 0.013 and 0.087 ± 0.010 for the gate-voltage shift and drain-source current change, respectively, Figure 6D) were also observed when using the lowest concentrations of recombinant 2019-nCoV spike protein inside artificial saliva. The difference is due to the less conductivity property of artificial saliva than that of PBS buffer. However, both groups of results demonstrate that our FET sensor is both highly sensitive and specific.

In the review of various sensing methods,[39,42,43,49−54] the FET approach has a lower LOD for SARS-CoV-2 in comparison with other approaches. In terms of VSTMs, both graphene and MXene−graphene have shown the lowest LOD for SARS-CoV-2 sensing (1 fg $mL^{-1}$). In addition, the MXene−graphene FET sensor reported in this paper has shown relatively high signal changes corresponding to the LOD. These results collectively demonstrated the promising virus-sensing performance of MXene−graphene VSTM, especially for H1N1 and SARS-CoV-2.

## 3. CONCLUSIONS

To conclude, we reported a novel MXene−graphene FET sensor for sensing both inactivated influenza A (H1N1) virus and SARS-CoV-2. The developed sensor is relatively easy to fabricate and of low-cost. We tested the sensing performance of the developed sensor with both H1N1 virus and recombinant 2019-nCoV spike protein. The results have shown a low LOD (125 copies/$mL^{-1}$ for H1N1 virus and 1 fg $mL^{-1}$ for recombinant 2019-nCoV spike protein) and a wide range of detection (up to 250,000 copies/$mL^{-1}$ for H1N1 virus and 10 pg $mL^{-1}$ for recombinant 2019-nCoV spike protein), as well as high specificity. It should be noted that the response time is about 50 ms, which is much faster than the existing detection approaches. The excellent performance of the developed sensor is attributed to the large number of surface-terminating groups of MXene, which offers a relatively large number of binding sites for APTES. Therefore, a relatively high number of viruses or protein linkers can be formed on MXene in comparison with VSTM that has non-covalently bonded probe linkers. It should be noted that the high signal-to-viral load (∼10% of current change at LODs for both H1N1 and SARS-CoV-2) demonstrates the ultra-high sensitivity of MXene−graphene FET for virus sensing. Potential applications include environmental virus sensing when a low viral load is present and wearable sensing when direct sample collection is not feasible.

## 4. EXPERIMENTAL SECTION

**4.1. Experimental Method.** The Raman spectrum was acquired using a Horiba LabRAM ARAMIS spectrometer with a 632.8 nm laser. AFM images were acquired on a Digital Instruments Nanoscope IIIA under tapping mode. The AFM tip was 6 nm in diameter and the cantilever was 2 N/m. The XRD (PANalytical, Philips MPD) results were acquired with Cu K<$\alpha$> radiation ($\lambda$ = 1.5406 Å) at $U$ = 45 kV and $I$ = 40 mA. FTIR data were obtained using a Nicolet 4700 FT-IR spectrometer. A 3D printer (Mega S) was used to print the clamping base using the fused deposition method with poly lactic acid material.

**4.2. Materials.** The inactivated influenza A (H1N1) virus was purchased from Microbiologics (St. Cloud, MN). The influenza A (H1N1) HA polyclonal antibody was purchased from Thermo Fisher Scientific (Waltham, MA). The recombinant 2019-nCoV spike protein S1 (His Tag) and SARS-CoV-2 spike antibody (Chimeric monoclonal antibody) were purchased from SinoBiological (Wayne, PA). Artificial saliva (ASTM E2720-16) with pH = 7 and 80 U/mL a-Amylase from *Aspergillus oryzae* were purchased from Pickering Laboratories (Mountain View, CA). The copper foil was purchased from Alfa Aesar (CAS: 7440-50-8, LOT no. P17D009). The $Ti_2AlC$ MAX phase (−325 mesh, particle size ≤ 45 $\mu$m) was purchased from Luoyang Tongrun Info Technology Co., Ltd. APTES was purchased from Sigma-Aldrich (Saint Louis, MO). Galinstan alloy (68.5% Ga, 21.5% In, 10% Sn) was purchased from Rotometals (San Leandro, CA).


https://dx.doi.org/10.1021/acsomega.0c05421
ACS Omega 2021, 6, 6643−6653

**4.3. Graphene on Glass Sample Preparation.** Large-area monolayer graphene was grown by CVD on 2 × 10 cm copper foils. During this process, gas species were fed into the reactor flow over a 25 $\mu$m thick piece of copper foil, where hydrocarbon precursors decomposed to carbon radicals at the copper surface and then formed monolayer graphene. To prepare graphene on a glass substrate (25 mm × 25 mm), a copper foil with graphene on top was spin-coated with a layer of polymethyl methacrylate (PMMA) (4000 rpm for 30 s). The foil was then etched away in 0.2 mol $L^{-1}$ $FeCl_3$ and 0.2 mol $L^{-1}$ $(NH_4)_2S_2O_8$ for 2 h. The remaining graphene/PMMA was cleaned with deionized (DI) water, transferred onto a glass substrate cleaned with acetone and baked at 120 °C for 15 min to get higher bonding. Finally, PMMA was removed by soaking in acetone solution, yielding a sample of graphene on the glass substrate. The residue of PMMA was removed by annealing at 400 °C in $N_2$. The Raman spectrum of monolayer graphene on Cu is shown in Figure S1 in Supporting Information.

**4.4. UV-Light Treatment on Prepared Graphene.** Ultraviolet (UV) light was applied to graphene to achieve partial oxidation and better bonding with MXene. The details are as follows. A high-pressure mercury lamp (total power, 240; radiant flux, 24 W for 240−320 nm; operating current, 4 A) was used as the UV-light source. The lamp was placed over the samples at a distance of 15−20 mm, resulting in the power density of light flux around 100 mW/$cm^2$. 5 min of UV treatment time was used. During the experiments, humidity in the chamber was maintained at 70−80%. After UV-light treatment, the resistance of graphene increased by 5%.

**4.5. MXene/Graphene on Glass Sample Preparation.** To remove Al from $Ti_2AlC$, chemical etching was conducted by slowly mixing 0.5 g of $Ti_2AlC$ into the etchant, prepared by dissolving 0.8 g of LiF in 10 mL of 6 M HCl. The mixture was stirred for 24 h at 35 °C, followed by repeated washing with DI water and centrifugation until the pH of supernatant reached 5.5−6.0. The $Ti_2CT_x$ aqueous colloidal solution was obtained via 5 min vortex shaking, followed by 1 h centrifugation at 3500 rpm. The obtained $Ti_2C$ colloidal solution (20 mg/mL) was coated onto graphene on glass using the interfacial film deposition method.[45] Briefly, about 50 mL of DI water was poured into a 100 mL glass beaker with a Teflon-coated magnetic stir bar. While vigorously stirring the DI water, 1 mL of $Ti_2C$ aqueous colloid was added into the glass vial. Under continued stirring, 6 mL of toluene was added into the vial and stirred vigorously for 20 min. Graphene on glass was placed near the bottom of another 600 mL glass beaker filled with 400 mL water. The stirred $Ti_2C$ MXene−toluene−water dispersion was quickly poured into the 600 mL glass beaker. The beaker was left still for 20 min to allow layering out of the emulsion and the formation of the interfacial film. After the formation of $Ti_2C$ thin film at the interface between water and toluene, graphene on glass was slowly lifted toward the top of the beaker while keeping its surface oriented parallel to the interface to obtain MXene/graphene on glass. Then, $N_2$ carrier gas blow over was applied for 5 min to remove toxic toluene.

**4.6. Fabrication of FET Devices and Experimental Setup of FET Characterization.** The fabrication of the microfluidic sensor in PDMS was accomplished through the use of the soft-lithography technique.[55] Lithographic patterning was implemented to fabricate master molds in a photoresist dry film (MM540, DuPont), which usually has a thickness equal to 35 $\mu$m.[56] At first, a layer of photoresist dry film was laminated onto a copper plate where a thermal laminator served the function for lamination purposes. Then, the copper plate along with a transparent photo mask (10,000 dpi, CAD/Art Services Inc.) was exposed to UV rays, and this process ultimately resulted in the development of the photo mask onto the copper plate, which was then rinsed in an aqueous solution of sodium carbonate and dried to obtain the master mold. Next, a PDMS mixture was prepared using a base and an initiator, degassed, and then cast on the master mold. Finally, the PDMS replica was peeled off from the master mold. To fabricate the microfluidic channel and electrode channels inside the PDMS chamber, PDMS chambers were laser-cut with 1.7 kW $CO_2$ laser using a Convergent Energy Arrow Ultimate model operating in a continuous wave mode at a wavelength of 10.6 $\mu$m. Several laser powers (100 W and 275 W), scanning speeds (from 2000 to140,000 mm/min), and modes (continuous mode and pulsed mode) were tried to cut channels with smooth edges and enough depth. Cross-section profiles of electrode channels cut with different parameters are shown in Figure S2. Finally, the liquid metal electrode channels were cut in one pass with a laser spot size of 1 mm, a laser power of 275 W, and a scanning speed of 6000 mm/min. Using the same laser parameters and spot size, the middle microfluidic channel was cut through in 16 passes. Between each pass, the laser was shut off for 30 s to minimize heat buildup and prevent damage to the PDMS. Then, the laser-cut PDMS chamber was bonded to the prepared sample. The details of the bonding process are shown in Figure S3. In short, first, the surface of the PDMS chamber was cleaned with tape and treated using corona (air plasma) for 5 min to remove contamination and increase the surface activity. Then, the PDMS chamber was punched onto the sample surface, followed by inserting the liquid metal (Galinstan, with 0 Ω resistance and 11 °C melting point) into the electrode channel using a syringe. To avoid solution leakage during FET testing and increase the efficiency, four samples were clamped between the acrylic plate and the 3D-printed clamping base plate.

A Keithley 4200 semiconductor characterization system was used to apply the gate and drain-source voltages and to measure the drain-source current. The FET was characterized using a two-electrode electrochemical cell. An Ag/AgCl electrode was used as the reference electrode to apply liquid-gating, while MXene−graphene was used as the working electrode. A 1× PBS buffer was used as an electrolyte while applying liquid-gating. The 1× PBS buffer contained 10 mM phosphate and 137 mM NaCl at pH 7.4. The source-drain voltage ($V_{DS}$) was kept at 2 V during all experiments.

**4.7. Immobilization of Antibody on $Ti_2C$ Surface.** APTES, which dissolves in ethanol (vol ratio, 1:50) was inserted into the solution channel and left for 4 h at room temperature to form an amide (OH−NH) bond between the amino terminals of APTES and hydroxyl terminal groups of MXene. Then, the solution channel was rinsed several times with ethanol and DI water to remove extra APTES. After that, the functionalized device was exposed to 10 $\mu$g $mL^{-1}$ influenza A (H1N1) HA polyclonal antibody or 250 $\mu$g $mL^{-1}$ SARS-CoV-2 spike antibody, which were prepared in PBS (1×, pH 7.4). 10 $\mu$L of the antibody solution was uniformly spread on the surface and incubated at 37 °C for 4 h, followed by washing with PBS containing Tween 20, water, and drying with $N_2$. After this process, a strong amide (NH−NH) bond was expected to form between the amino-terminating groups of APTES and antibody. Finally, BSA solution (1 mg $mL^{-1}$)


https://dx.doi.org/10.1021/acsomega.0c05421
ACS Omega 2021, 6, 6643−6653

was spread on the surface and incubated at 37 °C for 2 h, to be used as a blocking agent to prevent non-specific binding of the antigen to the VSTM. The sample surface was then washed with PBS and water and used for inactivated influenza A (H1N1) or recombinant 2019-nCoV spike protein [prepared in PBS (1×, pH 7.4)] capture.

## ■ ASSOCIATED CONTENT

### Supporting Information

The Supporting Information is available free of charge at https://pubs.acs.org/doi/10.1021/acsomega.0c05421.

Raman spectrum for monolayer graphene on Cu; $CO_2$ laser cutting of PDMS; $CO_2$ laser cutting experimental setup, depth profiles for PDMS channels under different laser cutting parameters; channel depth results for different cutting parameters; PDMS bonding process; and corona treatment of PDMS surface and bonding to MXene−graphene (PDF)

## ■ AUTHOR INFORMATION


### Corresponding Authors

**DongHyun Kim** − *Department of Electrical and Computer Engineering, Missouri University of Science and Technology, Rolla, Missouri 65401, United States*; Email: dkim@mst.edu

**Chenglin Wu** − *Department of Civil, Architectural, and Environmental Engineering, Missouri University of Science and Technology, Rolla, Missouri 65409, United States*; orcid.org/0000-0001-7733-1084; Email: wuch@mst.edu

### Authors

**Yanxiao Li** − *Department of Civil, Architectural, and Environmental Engineering, Missouri University of Science and Technology, Rolla, Missouri 65409, United States*

**Zhekun Peng** − *Department of Electrical and Computer Engineering, Missouri University of Science and Technology, Rolla, Missouri 65401, United States*

**Natalie J. Holl** − *Department of Biological Sciences, Missouri University of Science and Technology, Rolla, Missouri 65409, United States*

**Md. Rifat Hassan** − *Department of Mechanical and Aerospace Engineering, Missouri University of Science and Technology, Rolla, Missouri 65409, United States*

**John M. Pappas** − *Department of Mechanical and Aerospace Engineering, Missouri University of Science and Technology, Rolla, Missouri 65409, United States*

**Congjie Wei** − *Department of Civil, Architectural, and Environmental Engineering, Missouri University of Science and Technology, Rolla, Missouri 65409, United States*

**Omid Hoseini Izadi** − *Department of Electrical and Computer Engineering, Missouri University of Science and Technology, Rolla, Missouri 65401, United States*

**Yang Wang** − *Department of Civil, Architectural, and Environmental Engineering, Missouri University of Science and Technology, Rolla, Missouri 65409, United States*

**Xiangyang Dong** − *Department of Mechanical and Aerospace Engineering, Missouri University of Science and Technology, Rolla, Missouri 65409, United States*

**Cheng Wang** − *Department of Mechanical and Aerospace Engineering, Missouri University of Science and Technology, Rolla, Missouri 65409, United States*

**Yue-Wern Huang** − *Department of Biological Sciences, Missouri University of Science and Technology, Rolla, Missouri 65409, United States*; orcid.org/0000-0003-1957-6459

Complete contact information is available at: https://pubs.acs.org/10.1021/acsomega.0c05421


### Author Contributions

Chenglin Wu, D.K., Y.-W.H., Cheng Wang, X.D., and Y.W. conceived and supervised the project and designed the experiments. Chenglin Wu guided the team and provided funding support. Y.L. synthesized graphene, MXene−graphene, performed characterization, FET testing, and data analysis. Z.P. and O.H.I. conducted FET testing and did data analysis. N.J.H. prepared virus and antibody samples. M.R.H. fabricated PDMS chambers. J.M.P. cut channels in the PDMS plate. Congjie Wei. prepared the figures and drew the molecular structures. All the authors discussed the results, wrote the paper, and commented on the paper.

### Notes

The authors declare no competing financial interest.

## ■ ACKNOWLEDGMENTS

Yanxiao Li, Congjie Wei, Xiangyang Dong, and Chenglin Wu gratefully acknowledge financial support of this work by the National Science Foundation through grant no. CMMI-1930881. These authors also acknowledge funding support from Mid-America Transportation Center and Missouri Department of Transportation.

## ■ REFERENCES


(1) CDC COVID Data Tracker. https://covid.cdc.gov/covid-data-tracker/#cases_totalcases (accessed Sept. 13, 2020).

(2) Gross Domestic Product. 2nd Quarter 2020 (Second Estimate); Corporate Profits, 2nd Quarter 2020 (Preliminary Estimate) www.bea.gov/news/2020/gross-domestic-product-2nd-quarter-2020-second-estimate-corporate-profits-2nd-quarter (accessed Sept. 13, 2020).

(3) Soleimani, M. Acute kidney injury in SARS-CoV-2 infection: direct effect of virus on kidney proximal tubule cells. *Int. J. Mol. Sci.* **2020**, *21*, 3275.

(4) Alberici, F.; Delbarba, E.; Manenti, C.; Econimo, L.; Valerio, F.; Pola, A.; Maffei, C.; Possenti, S.; Gaggia, P.; Movilli, E.; Bove, S.; Malberti, F.; Farina, M.; Bracchi, M.; Costantino, E. M.; Bossini, N.; Gaggiotti, M.; Scolari, F. Management of patients on dialysis and with kidney transplant during COVID-19 coronavirus infection. *KIDNEYS* **2020**, *9*, 117−120.

(5) Vitiello, A.; Pelliccia, C.; Ferrara, F. COVID-19 patients with pulmonary fibrotic tissue: clinical pharmacological rational of antifibrotic therapy. *SN Compr. Clin. Med.* **2020**, *2*, 1709−1712.

(6) Kurapati, R.; Kostarelos, K.; Prato, M.; Bianco, A. Biomedical uses for 2D materials beyond graphene: current advances and challenges ahead. *Adv. Mater.* **2016**, *28*, 6052−6074.

(7) Liu, S.; Zhang, X.-d.; Gu, X.; Ming, D. Photodetectors based on two dimensional materials for biomedical application. *Biosens. Bioelectron.* **2019**, *143*, 111617.

(8) Jayakumar, A.; Surendranath, A.; Pv, M. 2D materials for next generation healthcare applications. *Int. J. Pharm.* **2018**, *551*, 309−321.

(9) Chimene, D.; Alge, D. L.; Gaharwar, A. K. Two-dimensional nanomaterials for biomedical applications: emerging trends and future prospects. *Adv. Mater.* **2015**, *27*, 7261−7284.

(10) Sinha, A.; Dhanjai, H.; Zhao, H.; Huang, Y.; Lu, X.; Chen, J.; Jain, R. An emerging material for sensing and biosensingr. *Trends Anal. Chem.* **2018**, *105*, 424−435.

(11) Guo, C.; Fan, L.; Wu, C.; Chen, G.; Li, W. Ultrasensitive LPFG corrosion sensor with Fe-C coating electroplated on a Gr/AgNW film. *Sens. Actuators, B* **2019**, *283*, 334−342.
(12) Pumera, M. Graphene in biosensing. *Mater. Today* **2011**, *14*, 308−315.
(13) Peña-Bahamonde, J.; Nguyen, H. N.; Fanourakis, S. K.; Rodrigues, D. F. Recent advances in graphene-based biosensor technology with applications in life sciences. *J. Nanobiotechnol.* **2018**, *16*, 75.
(14) Bai, Y.; Xu, T.; Zhang, X. Graphene-based biosensors for detection of biomarkers. *Micromachines* **2020**, *11*, 60.
(15) Tsang, D. K. H.; Lieberthal, T. J.; Watts, C.; Dunlop, I. E.; Ramadan, S.; Armando, E.; Klein, N. Chemically functionalised graphene FET biosensor for the label-free sensing of exosomes. *Sci. Rep.* **2019**, *9*, 13946.
(16) Novoselov, K. S.; Geim, A. K.; Morozov, S. V.; Jiang, D.; Zhang, Y.; Dubonos, S. V.; Grigorieva, I. V.; Firsov, A. A. Electric field effect in atomically thin carbon films. *Science* **2004**, *306*, 666−669.
(17) Dreyer, D. R.; Ruoff, R. S.; Bielawski, C. W. From conception to realization: an historial account of graphene and some perspectives for its future. *Angew. Chem., Int. Ed.* **2010**, *49*, 9336−9344.
(18) Szabó, T.; Berkesi, O.; Forgó, P.; Josepovits, K.; Sanakis, Y.; Petridis, D.; Dékány, I. Evolution of surface functional groups in a series of progressively oxidized graphite oxides. *Chem. Mater.* **2006**, *18*, 2740−2749.
(19) Gao, W.; Alemany, L. B.; Ci, L.; Ajayan, P. M. New insights into the structure and reduction of graphite oxide. *Nat. Chem.* **2009**, *1*, 403−408.
(20) Scida, K.; Stege, P. W.; Haby, G.; Messina, G. A.; García, C. D. Recent applications of carbon-based nanomaterials in analytical chemistry: critical review. *Anal. Chim. Acta* **2011**, *691*, 6−17.
(21) Mao, S.; Lu, G.; Yu, K.; Bo, Z.; Chen, J. Specific protein detection using thermally reduced graphene oxide sheet decorated with gold nanoparticle-antibody conjugates. *Adv. Mater.* **2010**, *22*, 3521−3526.
(22) Georgakilas, V.; Tiwari, J. N.; Kemp, K. C.; Perman, J. A.; Bourlinos, A. B.; Kim, K. S.; Zboril, R. Noncovalent functionalization of graphene and graphene oxide for energy materials, biosensing, catalytic, and biomedical applications. *Chem. Rev.* **2016**, *116*, 5464−5519.
(23) Naguib, M.; Mochalin, V. N.; Barsoum, M. W.; Gogotsi, Y. 25th anniversary article: MXenes: a new family of two-dimensional materials. *Adv. Mater.* **2014**, *26*, 992−1005.
(24) Anasori, B.; Lukatskaya, M. R.; Gogotsi, Y. 2D metal carbides and nitrides (MXenes) for energy storage. *Nat. Rev. Mater.* **2017**, *2*, 16098.
(25) Riazi, H.; Anayee, M.; Hantanasirisakul, K.; Shamsabadi, A. A.; Anasori, B.; Gogotsi, Y.; Soroush, M. Surface modification of a MXene by an aminosilane coupling agent. *Adv. Mater. Interfaces* **2020**, *7*, 1902008.
(26) Xu, B.; Zhi, C.; Shi, P. Latest advances in MXene biosensors. *JPhys Mater.* **2020**, *3*, 031001.
(27) Kim, S. J.; Koh, H.-J.; Ren, C. E.; Kwon, O.; Maleski, K.; Cho, S.-Y.; Anasori, B.; Kim, C.-K.; Choi, Y.-K.; Kim, J.; Gogotsi, Y.; Jung, H.-T. Metallic $Ti_3C_2T_x$ MXene gas sensors with ultrahigh signal-to-noise ratio. *ACS Nano* **2018**, *12*, 986−993.
(28) Driscoll, N.; Richardson, A. G.; Maleski, K.; Anasori, B.; Adewole, O.; Lelyukh, P.; Escobedo, L.; Cullen, D. K.; Lucas, T. H.; Gogotsi, Y.; Vitale, F. Two-dimensional $Ti_3C_2$ MXene for high-resolution neural interfaces. *ACS Nano* **2018**, *12*, 10419−10429.
(29) Szuplewska, A.; Kulpińska, D.; Dybko, A.; Jastrzębska, A. M.; Wojciechowski, T.; Rozmysłowska, A.; Chudy, M.; Grabowska-Jadach, I.; Ziemkowska, W.; Brzózka, Z.; Olszyna, A. 2D $Ti_2C$ (MXene) as a novel highly efficient and selective agent for photothermal therapy. *Mater. Sci. Eng., C* **2019**, *98*, 874−886.
(30) Ravina; Dalal, A.; Mohan, H.; Prasad, M.; Pundir, C. S. Detection methods for influenza A H1N1 virus with special reference to biosensors: a review. *Biosci. Rep.* **2020**, *40*, BSR20193852.
(31) Ahmed, S. R.; Kim, J.; Tran, V. T.; Suzuki, T.; Neethirajan, S.; Lee, J.; Park, E. Y. In situ self-assembly of gold nanoparticles on hydrophilic and hydrophobic substrates for influenza virus-sensing platform. *Sci. Rep.* **2017**, *7*, 44495.
(32) Lee, K. G.; Lee, T. J.; Jeong, S. W.; Choi, H. W.; Heo, N. S.; Park, J. Y.; Park, T. J.; Lee, S. J. Development of a plastic-based microfluidic immunosensor chip for detection of H1N1 influenza. *Sensors* **2012**, *12*, 10810−10819.
(33) Critchley, P.; Dimmock, N. J. Binding of an influenza A virus to a neomembrane measured by surface plasmon resonance. *Bioorg. Med. Chem.* **2004**, *12*, 2773−2780.
(34) Su, L.-C.; Chang, C.-M.; Tseng, Y.-L.; Chang, Y.-F.; Li, Y.-C.; Chang, Y.-S.; Chou, C. Rapid and highly sensitive method for influenza A (H1N1) virus detection. *Anal. Chem.* **2012**, *84*, 3914−3920.
(35) Nidzworski, D.; Pranszke, P.; Grudniewska, M.; Król, E.; Gromadzka, B. Universal biosensor for detection of influenza virus. *Biosens. Bioelectron.* **2014**, *59*, 239−242.
(36) Hai, W.; Goda, T.; Takeuchi, H.; Yamaoka, S.; Horiguchi, Y.; Matsumoto, A.; Miyahara, Y. Specific recognition of human influenza virus with PEDOT bearing sialic acid-terminated trisaccharides. *ACS Appl. Mater. Interfaces* **2017**, *9*, 14162−14170.
(37) Nidzworski, D.; Siuzdak, K.; Niedziałkowski, P.; Bogdanowicz, R.; Sobaszek, M.; Ryl, J.; Weiher, P.; Sawczak, M.; Wnuk, E.; Goddard, W. A.; Jaramillo-Botero, A.; Ossowski, T. A rapid-response ultrasensitive biosensor for influenza virus detection using antibody modified boron-doped diamond. *Sci. Rep.* **2017**, *7*, 1−10.
(38) Lee, W.; Kang, T.; Kim, S.-H.; Jeong, J. An antibody-immobilized silica inverse opal nanostructure for label-free optical biosensors. *Sensors* **2018**, *18*, 307.
(39) Lee, D.; Chander, Y.; Goyal, S. M.; Cui, T. Carbon nanotube electric immunoassay for the detection of swine influenza virus H1N1. *Biosens. Bioelectron.* **2011**, *26*, 3482−3487.
(40) Bai, C.; Lu, Z.; Jiang, H.; Yang, Z.; Liu, X.; Ding, H.; Li, H.; Dong, J.; Huang, A.; Fang, T.; Jiang, Y.; Zhu, L.; Lou, X.; Li, S.; Shao, N. Aptamer selection and application in multivalent binding-based electrical impedance detection of inactivated H1N1 virus. *Biosens. Bioelectron.* **2018**, *110*, 162−167.
(41) Mikuła, E.; Silva, C. E.; Kopera, E.; Zdanowski, K.; Radecki, J.; Radecka, H. Highly sensitive electrochemical biosensor based on redox - active monolayer for detection of anti-hemagglutinin antibodies against swine-origin influenza virus H1N1 in sera of vaccinated mice. *BMC Vet. Res.* **2018**, *14*, 328.
(42) Torrente-Rodríguez, R. M.; Lukas, H.; Tu, J.; Min, J.; Yang, Y.; Xu, C.; Rossiter, H. B.; Gao, W. SARS-CoV-2 rapidplex: A graphene-based multiplexed telemedicine platform for rapid and low-cost COVID-19 diagnosis and monitoring. *Matter* **2020**, *3*, 1981−1998.
(43) Seo, G.; Lee, G.; Kim, M. J.; Baek, S.-H.; Choi, M.; Ku, K. B.; Lee, C.-S.; Jun, S.; Park, D.; Kim, H. G.; Kim, S.-J.; Lee, J.-O.; Kim, B. T.; Park, E. C.; Kim, S. I. Rapid detection of COVID-19 causative virus (SARS-CoV-2) in human nasopharyngeal swab specimens using field-effect transistor-based biosensor. *ACS Nano* **2020**, *14*, 5135−5142.
(44) Li, Y.; Huang, S.; Wei, C.; Wu, C.; Mochalin, V. N. Adhesion of two-dimensional titanium carbides (MXenes) and graphene to silicon. *Nat. Commun.* **2019**, *10*, 1−8.
(45) Dong, Y.; Chertopalov, S.; Maleski, K.; Anasori, B.; Hu, L.; Bhattacharya, S.; Rao, A. M.; Gogotsi, Y.; Mochalin, V. N.; Podila, R. Saturable absorption in 2D $Ti_3C_2$ MXene thin films for passive photonic diodes. *Adv. Mater.* **2018**, *30*, 1705714.
(46) Ji, J.; Zhao, L.; Shen, Y.; Liu, S.; Zhang, Y. Covalent stabilization and functionalization of MXene via silylation reactions with improved surface properties. *FlatChem* **2019**, *17*, 100128.
(47) Kumar, S.; Lei, Y.; Alshareef, N. H.; Quevedo-Lopez, M. A.; Salama, K. N. Biofunctionalized two-dimensional $Ti_3C_2$ MXenes for ultrasensitive detection of cancer biomarker. *Biosens. Bioelectron.* **2018**, *121*, 243−249.
(48) Pak, S.; Jang, A.-R.; Lee, J.; Hong, J.; Giraud, P.; Lee, S.; Cho, Y.; An, G.-H.; Lee, Y.-W.; Shin, H. S.; Morris, S. M.; Cha, S.; Sohn, J.


https://dx.doi.org/10.1021/acsomega.0c05421
*ACS Omega* 2021, 6, 6643−6653

I.; Kim, J. M. Surface functionalization-induced photoresponse characteristics of monolayer $MoS_2$ for fast flexible photodetectors. *Nanoscale* **2019**, *11*, 4726−4734.
(49) Qiu, G.; Gai, Z.; Tao, Y.; Schmitt, J.; Kullak-Ublick, G. A.; Wang, J. Dual-functional plasmonic photothermal biosensors for highly accurate severe acute respiratory syndrome coronavirus 2 detection. *ACS Nano* **2020**, *14*, 5268−5277.
(50) Park, C.; Choi, W.; Kim, D.; Jin, B.; Lee, J.-S. Highly sensitive detection of influenza A (H1N1) virus with silicon nanonet bioFETs. *IEEE Sens. J.* **2019**, *19*, 10985−10990.
(51) Gao, A.; Lu, N.; Dai, P.; Li, T.; Pei, H.; Gao, X.; Gong, Y.; Wang, Y.; Fan, C. Silicon-nanowire-based CMOS-compatible field-effect transistor nanosensors for ultrasensitive electrical detection of nucleic acids. *Nano Lett.* **2011**, *11*, 3974−3978.
(52) Hideshima, S.; Hayashi, H.; Hinou, H.; Nambuya, S.; Kuroiwa, S.; Nakanishi, T.; Momma, T.; Nishimura, S.-I.; Sakoda, Y.; Osaka, T. Glycan-immobilized dual-channel field effect transistor biosensor for the rapid identification of pandemic influenza viral particles. *Sci. Rep.* **2019**, *9*, 1−10.
(53) Hideshima, S.; Hinou, H.; Ebihara, D.; Sato, R.; Kuroiwa, S.; Nakanishi, T.; Nishimura, S.-I.; Osaka, T. Attomolar detection of influenza A virus hemagglutinin human H1 and avian H5 using glycan-blotted field effect transistor biosensor. *Anal. Chem.* **2013**, *85*, 5641−5644.
(54) Lu, N.; Gao, A.; Zhou, H.; Wang, Y.; Yang, X.; Wang, Y.; Li, T. Progress in silicon nanowire-based field-effect transistor biosensors for label-free detection of DNA. *Chin. J. Chem.* **2016**, *34*, 308−316.
(55) McDonald, J. C.; Duffy, D. C.; Anderson, J. R.; Chiu, D. T.; Wu, H.; Schueller, O. J. A.; Whitesides, G. M. Fabrication of microfluidic systems in poly (dimethylsiloxane). *Electrophoresis* **2000**, *21*, 27−40.
(56) Zhou, R.; Wang, C. Acoustic bubble enhanced pinched flow fractionation for microparticle separation. *J. Micromech. Microeng.* **2015**, *25*, 084005.


https://dx.doi.org/10.1021/acsomega.0c05421
*ACS Omega* 2021, 6, 6643−6653